ELSEVIER

Rational design of positive-hexagon-shaped two-dimensional ZIF-derived materials as improved bifunctional oxygen electrocatalysts for use as long-lasting rechargeable Zn–Air batteries

Yi Guan, Yongliang Li*, Shan Luo, Xiangzhong Ren*, Libo Deng, Lingna Sun, Hongwei Mi, Peixin Zhang, Jianhong Liu

College of Chemistry and Environmental Engineering, Shenzhen University, Shenzhen, Guangdong 518060, PR China

ABSTRACT

Herein, a bottom-up method, i.e., a surfactant-assisted synthetic method to synthesize a novel dual-metal (Co/Zn) zeolitic-imidazolate framework (ZIF) that could maintain its positive-hexagon-shaped morphology after high-temperature thermal treatment, has been developed. As a bifunctional electrocatalyst, the Co nanoparticles encapsulated into both nitrogen-doped positive-hexagon-shaped carbon nanosheets and carbon nanotubes distributed over the nanosheet surface (Co-*N*-PHCNTs) show excellent electrocatalytic performance, superior to that of state-of-the-art benchmark noble-metal electrocatalysts. Remarkably, in a practical demonstration, the Co-*N*-PHCNTs serve as bifunctional air electrodes for Zn–air batteries, exhibiting a high peak power density of ≈ 125.41 mW cm^{-2} at a current density of ≈ 130 mA cm^{-2} with an extraordinary charge-discharge cyclability of over 673 h at 5 mA cm^{-2}. This strategy not only provides guidance for the synthesis of 2D ZIF-derived materials but also for other 2D materials in cross-cutting applications.

1. Introduction

To solve the ever-increasing serious environmental degradation issue and the urgent energy depletion problem, considerable effort has been made to develop clean and sustainable energy sources [1–3]. Due to the high theoretical energy density, low cost, and improved safety, rechargeable metal-air batteries are considered as one of the most promising energy storage systems [4,5]. As the fourth most earth-abundant metal, Zn is a promising anode material for metal-air batteries [6–8]. However, there is still a critical challenge for Zn–air battery technology because an effective and stable bifunctional air electrode has not yet been developed. Although noble metals such as Pt, Ir, and Ru are the best-known electrocatalysts for the oxygen reduction reaction (ORR) and oxygen evolution reaction (OER) for this battery system, their high cost and poor stability hinder the practical application and commercialization of these systems [9–12].

With increasing concern regarding transition metal particles encapsulated into carbonaceous materials, a number of studies have demonstrated that these composites have high potential to be suitable alternatives to noble metals, which perform high activity and long-term stability for the ORR and OER [13–15]. The carbon layer on the surface

not only prevents transition metal particles from aggregating and from directly contacting the reactants and electrolyte solutions [16,17], but also increases the electron transport in the composite [18]. In addition, the doping of heteroatoms (e.g., B, N, P) into carbon lattices could further optimize the surface electronic distribution and play a synergetic role in facilitating the electrocatalytic kinetic processes [19–21]. Zeolitic imidazolate frameworks (ZIFs) have been used to fabricate heteroatom-doped nanocarbon due to their low cost, tailorable structures, and nitrogen self–doping [22–25]. Additionally, two-dimensional (2D) ZIFs have attracted significant interest because their counterparts could be a good choice as precursors to prepare carbon materials [26,27]. Although 2D ZIFs can be synthesized by bottom-up methods (directly synthesized from metal ions and ligands), most pyrolysis products derived from ZIFs lose their structural stability and become amorphous carbon [28–30]. Therefore, novel strategies to effectively control the synthesis of 2D materials derived from 2D ZIFs are extremely desirable.

Herein, we report a bottom-up method, i.e., a surfactant-assisted method, to synthesize novel dual-metal (Co/Zn) ZIFs that can maintain their positive-hexagon-shaped morphology (denoted as ZIF-PHS) after high-temperature thermal treatment. The Co nanoparticles are

---

* Corresponding authors.
  E-mail addresses: liyli@szu.edu.cn (Y. Li), renxz@szu.edu.cn (X. Ren).

encapsulated not only into nitrogen-doped positive-hexagon-shaped carbon nanosheets, but also in the carbon nanotubes (CNTs) which are distributed over the surface of the nanosheet (denoted as Co-*N*-PHCNTs). The carbon nanotubes grown from the nanosheets are critical to improving the electrochemical performance, which can not only enhance the conductivity and maintain the structural integrity but also promote active site exposure through encapsulated Co nanoparticles. The 2D ZIFs derived nanosheet structures may provide favourable interaction between active sites and substrate molecules with a smaller diffusion barrier which will increase the effective electrochemical active surface area [31–34]. Besides, the uniquely intertwined and macroporous features of CNTs not only greatly facilitate the electron transport and favourable absorption of the reaction intermediates, but also make the material present a large specific surface area, which highly contribute to the catalytic activity [35]. In addition, the high-angle annular dark field-scanning transmission electron microscopy (HAADF-STEM) combined with X-ray photoelectron spectroscopy (XPS) demonstrates that the Co nanoparticles have a symbiotic relationship with the nearby N atoms. In this way, the Co-*N*-C moieties as active sites in the material which resulted from the unique sheet-derived carbon nanotube structure synergized with strong covalent bonds between Co and N can also contribute to the excellent electrocatalytic activity and long-term stability. More importantly, the rechargeable Zn-air battery that uses Co-*N*-PHCNTs as an air electrode exhibits a high peak power density ($\approx 125.41 \, mW \, cm^{-2}$ at a current density of $\approx 130 \, mA \, cm^{-2}$), a low charge–discharge gap ($\approx 0.796 \, V$ at $5 \, mA \, cm^{-2}$) and long-term stability (over $673 \, h$ at $5 \, mA \, cm^{-2}$).

2. Experimental section

2.1. Synthesis of Co/Zn (1:1) ZIF-PHS

$Zn(Ac)_2$ and $Co(NO_3)_2 \cdot 6H_2O$ with a molar ratio of 1:1 were dissolved in $40 \, mL$ of deionized water, denoted as solution A. Then, 2-methylimidazole (2-mIm) and polyvinyl pyrrolidone (PVP) were added to another $40 \, mL$ of deionized water, denoted as solution B. Solution A and solution B were mixed and placed in a $60 \, °C$ water bath for $3 \, h$ with vigorous stirring. The reacted solution was then stirred for $12 \, h$ and subsequently collected by centrifugation. After drying in a vacuum oven at $60 \, °C$ for $12 \, h$, Co/Zn (1:1) ZIF-PHS was obtained. The details of other samples can be found in Table S1 (Supporting Information).

2.2. Synthesis of Co-N-PHCNTs

Typically, $500 \, mg$ of Co/Zn (1:1) ZIF-PHS was heated to $900 \, °C$ in N_2 for $2 \, h$ with a ramping rate of $5 \, °C \, min^{-1}$. The Co-*N*-PHCNTs were collected after the furnace was naturally cooled to room temperature,.

2.3. Preparation of the working electrode

A mixture of $5 \, mg$ of samples and $40 \, \mu L$ 5 wt% Nafion solution were dispersed into $1.5 \, mL$ of ethanol and it was ultrasonicating for $30 \, min$. Then, $15 \, \mu L$ of electrocatalyst ink was dropping on a glassy carbon RRDE disk ($\Phi = 4 \, mm$, $A_{disk} = 0.126 \, cm^2$; inner/outer-ring diameter: $5.0/7.0 \, mm$, $A_{ring} = 0.188 \, cm^2$) from BAS Inc and the electrocatalyst loading was $0.398 \, mg \, cm^{-2}$.

2.4. Electrochemical evaluations

The electrochemical measurements were performed in a three-electrode system using the Ag/AgCl (saturated KCl) as reference electrode and the Pt wire as a counter electrode, respectively. All potential values were calibrated to reversible hydrogen electrode (RHE). The temperature of electrochemical measurements was kept at $25 \, °C$. The Linear sweep voltammograms (LSV) tests were acquired at various rotation rates ranging from 625 to 2025 rpm with a scan rate of $5 \, mV \, s^{-1}$.

The accelerated durability tests were conducted in O_2-saturated $0.1 \, M$ KOH solution with a potential range of $0.4–1.0 \, V$ and $1.2–1.8 \, V$ at a sweep rate of $100 \, mV \, s^{-1}$ for ORR and OER, respectively. The $3 \, M$ methanol and CO (10 vol %) were introduced into the electrolyte during the i-t stability tests for ORR, respectively. The commercial 20 wt% Pt/C ($20 \, \mu g_{Pt} \, cm^{-2}$) and RuO_2 ($0.1 \, mg \, cm^{-2}$) were served as benchmarking electrocatalysts for ORR and OER, respectively. The electrochemical double layer capacitances (C_{dl}) of electrocatalysts were measured by CV method and a potential range of $1.065–1.135 \, V$ was selected for the capacitance measurements.

2.5. Zinc–Air battery tests

The zinc-air battery performance was evaluated in homemade cells. The Air cathodes were constructed by dispersing the electrocatalysts on $1.5 \, cm \times 5 \, cm$ carbon paper with a loading of $1.0 \, mg \, cm^{-2}$, the anode was zinc foil and the electrolyte was a solution of $0.2 \, M$ zinc acetate in $6.0 \, M$ KOH. For comparison, the electrocatalyst made from Pt/C and RuO_2 (1:1 wt./wt.) was used as reference electrode. Galvanostatic discharge and charge cycling of the Zn–air batteries were performed through a recurrent galvanostatic pulse method at a current density of 5 or $10 \, mA \, cm^{-2}$ with 20 min per cycle (10 min for charge and 10 min for discharge). These galvanostatic charge/discharge curves were recorded using a LAND battery testing station (CT2001A) at room temperature. Polarization data were collected using the LSV method at a scan rate of $5 \, mV \, s^{-1}$ with cut-off voltages of $0.5 \, V$ for the discharge curves and $3.0 \, V$ for the charge curves.

3. Results and discussion

3.1. Synthesis and characterization

To obtain the Co-*N*-PHCNTs, the precursor was first synthesized based on the strong interactions between surfactants and nanocrystal particles [36], which is illustrated in Fig. 1a. First, a given amount of Co^{2+} and Zn^{2+} was mixed with 2-mIm and PVP in an aqueous solution at $60 \, °C$ for $3 \, h$ to form an intermediate product (**Fig. S1**). Then, the aqueous solution was stirred for $12 \, h$ at room temperature to obtain the ZIF-PHS (Fig. 1b). After pyrolysis of Co/Zn (1:1) ZIF-PHS at $900 \, °C$ for $2 \, h$ in N_2 atmosphere, the Co-*N*-PHCNTs can be synthesized, which show a unique morphology of positive-hexagon-shaped nanosheets covered with carbon nanotubes (Fig. 1c and d). Notably, in this bottom-up method, the coordination effect between the Zn^{2+} and Co^{2+} sites on the surface of Co/Zn ZIF-PHS polyhedra and the hydrophilic groups of the surfactants will decrease the crystal growth rate and control the crystal size as well as the morphology [37,38]. Additionally, PVP, as an encapsulating agent, can effectively inhibit the vertical growth of MOFs, resulting in a 2D morphology [27,39]. To demonstrate that the PVP plays an important role in maintaining the 2D ZIF morphology after high temperature pyrolysis, the Co-*N*-PHCNTs without PVP have been prepared (**Fig. S2**). In addition, in the following pyrolysis procedure, the cohesive interactions between the selected surfactant and Co/Zn ZIF-PHS lead to a unique confinement effect to avoid the collapse of the 2D regular hexagonal layer structure while also mitigating the agglomeration of neighbouring Co nanoparticles [40]. By means of transmission electron microscopy (TEM), it was observed that the Co nanoparticles were distributed in the carbon nanosheets (**Fig. S3a and b**) and encapsulated in the CNTs derivative from the carbon layer (Fig. 1e).High-resolution TEM (HR-TEM) confirms that the Co nanoparticles are crystalline and the interplanar distance to the lattice fringes is ~2.05 Å, which matches the β-Co (111) facets. Furthermore, a d-spacing of 3.7 Å corresponding to the (002) plane of graphite carbon can be found around the Co nanoparticle (Fig. 1f). In addition, Figs. 1g and **S3** demonstrate that the N species coexist with the Co nanoparticles across the CNTs and are also distributed on the carbon layer, as determined by high-angle annular dark field-scanning transmission
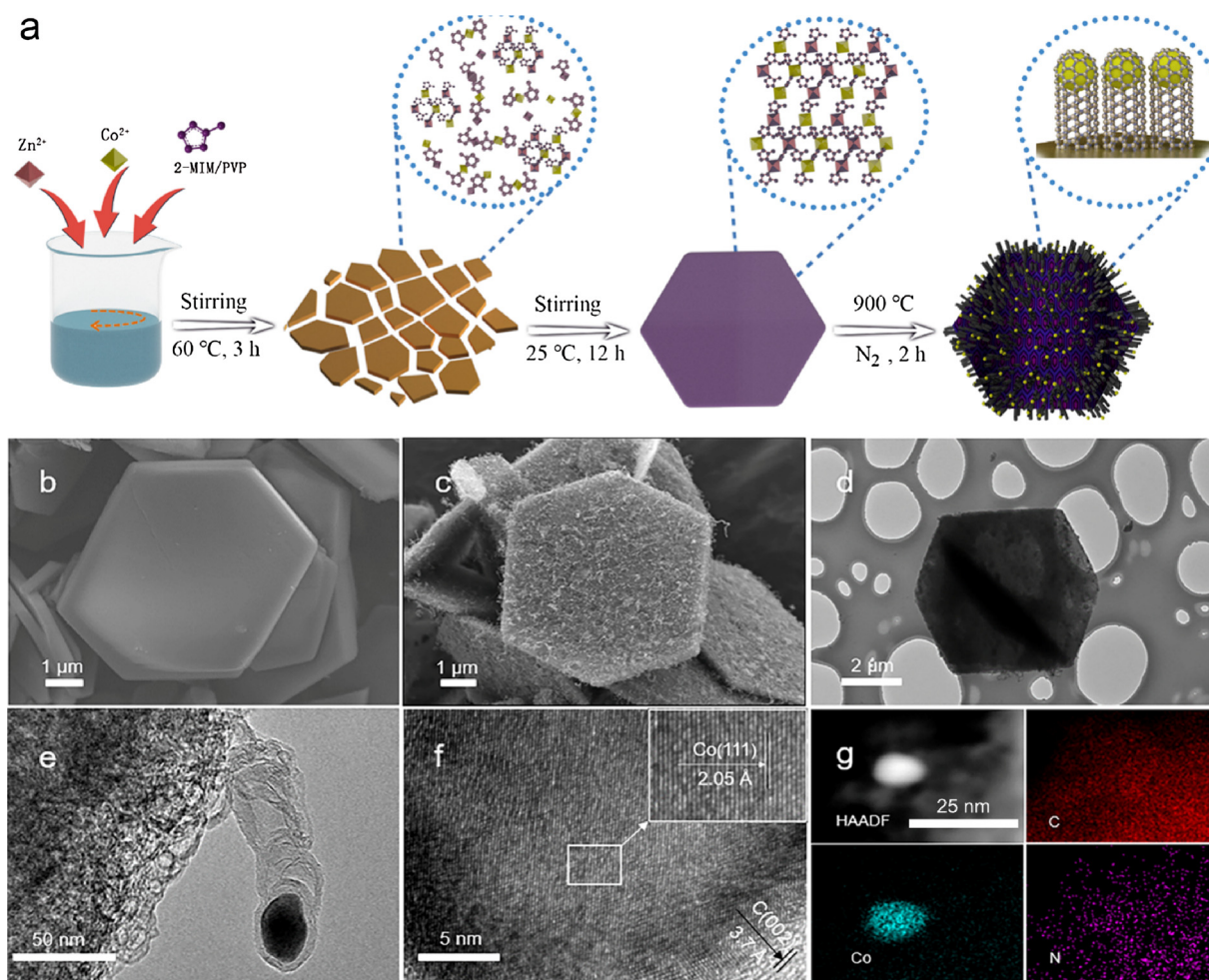
Fig. 1. (a) Schematic illustration of the synthesis of Co-*N*-PHCNTs. SEM images of (b) Co/Zn (1:1) ZIF-PHS and (c) its resultant Co-*N*-PHCNTs. TEM images of (d) Co-*N*-PHCNTs and (e) the Co encapsulated in the tips of the CNT derivative from the carbon layer (f) HRTEM images of Co-*N*-PHCNTs. (g) HAADF-STEM image and the EDS mapping of Co/Zn (1:1) ZIF-PHS-derived Co-*N*-PHCNTs.

electron microscopy (HAADF-STEM) and the corresponding EDS mapping. In this way, the Co-*N*-C moieties as active sites could make a great contribution to improving the electrocatalytic performance [41–43].

To successfully prepare 2D ZIFs, which can maintain two-dimensional morphology after calcination at high temperature, it is inspired by the strong interactions between surfactants and nanocrystal particles in solution phases, as mentioned above. However, if the synthesis involves only a process at room temperature for 15 h without the reaction at 60 °C for 3 h, even the product can exhibit a 2D layer morphology (denoted as Co/Zn ZIF-L), but the pyrolysis product Co-*N*-CNT cannot maintain the morphology of ZIFs after pyrolysis (**Fig. S4a** and **b**). This is because the lack of stirring in the water bath at 60 °C leads to the inability of PVP to function as a morphological stabilizer during the binding of dimethylimidazole ligands to metal salt ions; therefore, the sample will lose its fixed shape and become amorphous carbon. In addition, the Co/Zn ZIF-PHS crystal is also regulated by changing the proportion of metal ions. With different ratios of Co and Zn ions, the synthesized ZIFs will show different morphologies and structures. By choosing pure Zn-ZIF-PHS and Co-ZIF-PHS as precursors, their pyrolysis products present unique morphologies. For pure Zn-ZIF-PHS, the pyrolysis product consists of nitrogen-doped irregular carbon nanoribbons (N-PHCNRs) while for Co-ZIF-PHS, the pyrolysis product consists of aggregated Co nanoparticles distributed in the nitrogen-doped irregular carbon nanosheets (Co/N-PHCNSs). Their morphologies and chemical components were investigated by SEM and X-ray diffraction (XRD), as shown in **Figs. S5** and **S6**. With a Co/Zn molar ratio of 1:4, the final

product will lose its positive-hexagon-shaped morphology, and a large number of small pieces accumulate and agglomerate to form a pine-cone-like appearance (**Fig. S7**). When the Co/Zn molar ratio is 1:2, the final product can maintain a positive-hexagon-shaped morphology but has less carbon nanotubes distributing on the surface than the sample with a Co/Zn ratio of 1:1 (**Fig. S8**). When the Co/Zn molar ratio changes to 2:1, the Co nanoparticles will aggregate with more Co due to the growth of CNTs (**Fig. S9**) [44]. The abovementioned phenomenon demonstrates the evaporation of Zn at high pyrolysis temperature accelerates the growth of CNT, and this process will be catalyzed by Co nanoparticles [45]. The proper Co/Zn ion ratio and suitable temperature treatment both play crucial roles in manufacturing this novel Co-*N*-PHCNT structure. It can also be concluded that an increase in the proportion of Co ions is conducive to the growth of carbon nanotubes and that an increase in the proportion of Zn ions will promote formation of the lamellar structure within a certain range.

According to the XRD patterns (Fig. 2a), the peaks at approximately 26.3° is relating to the (002) plane of the graphitic carbon [15]. In addition, the peak intensity of (002) plane is higher in Co-*N*-PHCNTs than that in Co/N-PHCNSs, which indicates that Co-*N*-PHCNTs have a higher degree of graphitization and better conductivity than Co/N-PHCNSs. Furthermore, the peak at ˜44.2° presenting both in the Co-*N*-PHCNT and Co/N-PHCNS samples corresponds to the (111) planes of β-Co (PDF #15-0806) [28], which is consistent with the HR-TEM results. The Raman spectra reveal two peaks, which can be regarded as a G-band ($˜1585 cm^{-1}$) for graphitic sp^2-hybridized carbon and a D-band
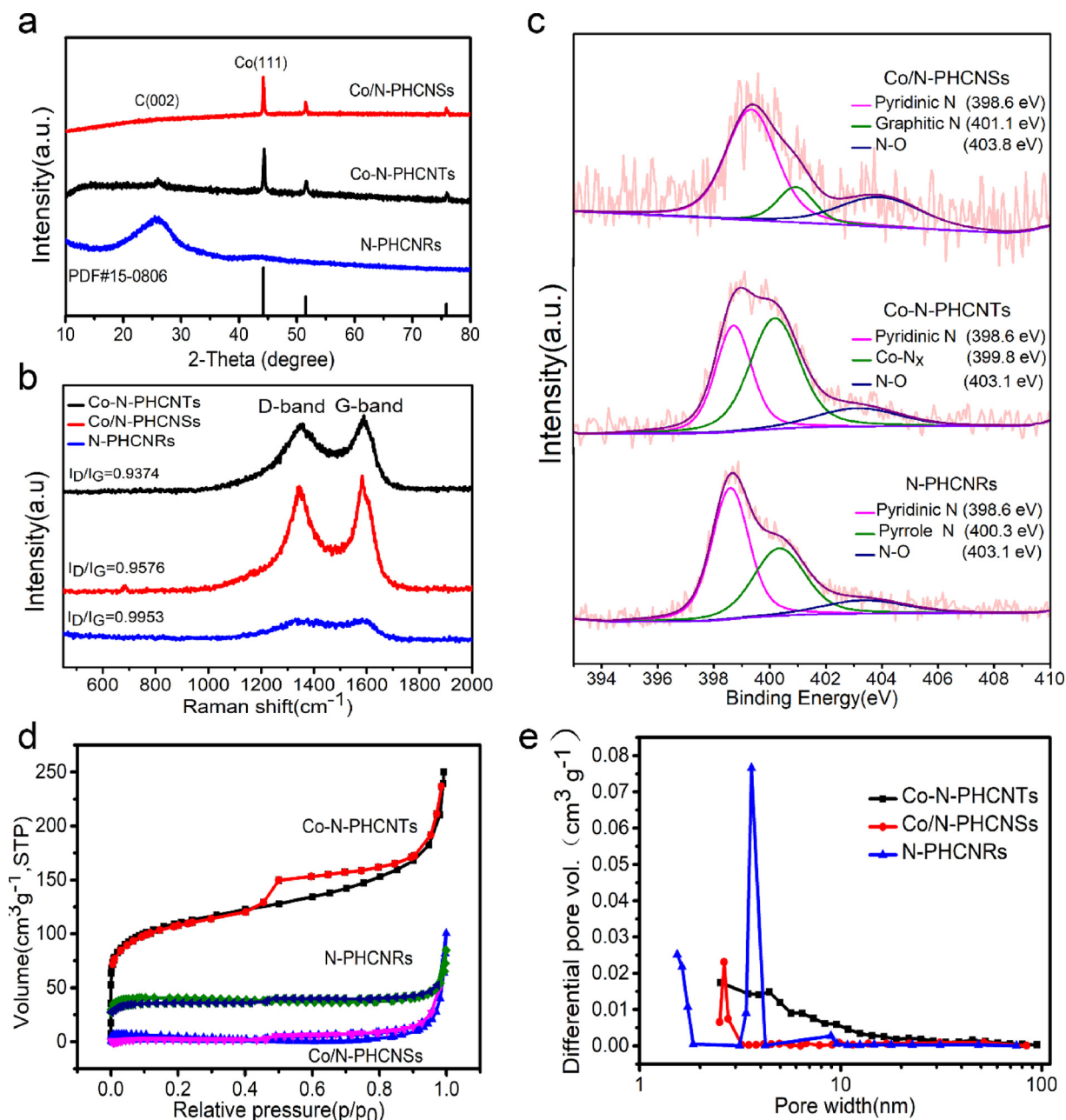
Fig. 2. (a) XRD patterns, (b) Raman spectra, (c) high-resolution N 1s XPS spectra, (d) N$_2$ adsorption–desorption isotherms and (e) the pore size distribution curves of the N-PHCNRs, Co-*N*-PHCNTs and Co/N-PHCNSs.

($\tilde{}$1345 cm^{-1}) for lattice defects (Fig. 2b) [46]. It is worth mentioning that the additional peak at $\tilde{}$675 cm^{-1} in the Raman spectrum of Co/N-PHCNSs is related to the Co species [47]. It can be seen that Co-*N*-PHCNTs have the lowest I$_D$/I$_G$ ratio among the three products, which demonstrates that Co-*N*-PHCNTs have the highest graphite carbon contents, indicating that the sample may possess high conductivity. In addition, no peak attributed to the Co species is observed for Co-*N*-PHCNTs, which indicates that the Co nanoparticles can be totally covered by the graphite carbon layer, of which the thickness can be at least 3 nm (**Fig. S10**) and beyond the limits of Raman detection ($\tilde{}$2 nm) [48].

XPS analysis was used to reveal the element electronic states in the products. **Fig. S11a–c** demonstrates that the three main peaks of the C 1s spectra for three products can be deconvoluted into C—C at $\tilde{}$284.7 eV, C=N at $\tilde{}$285.6 eV and C—O at $\tilde{}$286.8 eV. [49,50] The Co 2p peak of Co-*N*-PHCNTs and Co/N-PHCNSs can be deconvoluted into three peaks of Co(0), Co 2p$_{3/2}$ and Co 2p$_{1/2}$ at $\tilde{}$778.5, 779.9 and 795.7 eV,

respectively, and also some satellites peaks (**Fig. S11d**) [51,52]. Additionally, the XPS and EDS mapping results reveal that the Zn species completely vanish due to vaporization of metallic Zn at approximately 800 °C, as shown in **Fig. S12** [53]. The high-resolution N1 s spectrum for Co-*N*-PHCNTs can be deconvoluted into three main peaks, corresponding to pyridinic N at 398.6 eV (36.8%) [54], Co-N$_x$ at approximately 399.8 eV (50%) [29] and N–O at approximately 403.1 eV (13.2%) (Fig. 2c). For Co/N-PHCNSs, the spectrum can be deconvoluted into peaks for pyridinic N at 398.6 eV, graphitic N at 401.1 eV and N–O at $\tilde{}$403.1 eV. Otherwise, the high-resolution N 1s spectrum for N-PHCNRs is deconvoluted into three main peaks of pyridinic N at$\tilde{}$398.6 eV, pyrrolic N at $\tilde{}$400.3 eV and N–O at $\tilde{}$403.1 eV [28,29]. The presence of Co-N$_x$ and its extremely high nitrogen content may improve the catalytic activity for Co-*N*-PHCNT sample, which also demonstrates that the covalent bonds between Co and pyrrolic N involve transfer of electrons from Co to N [29,55–57].
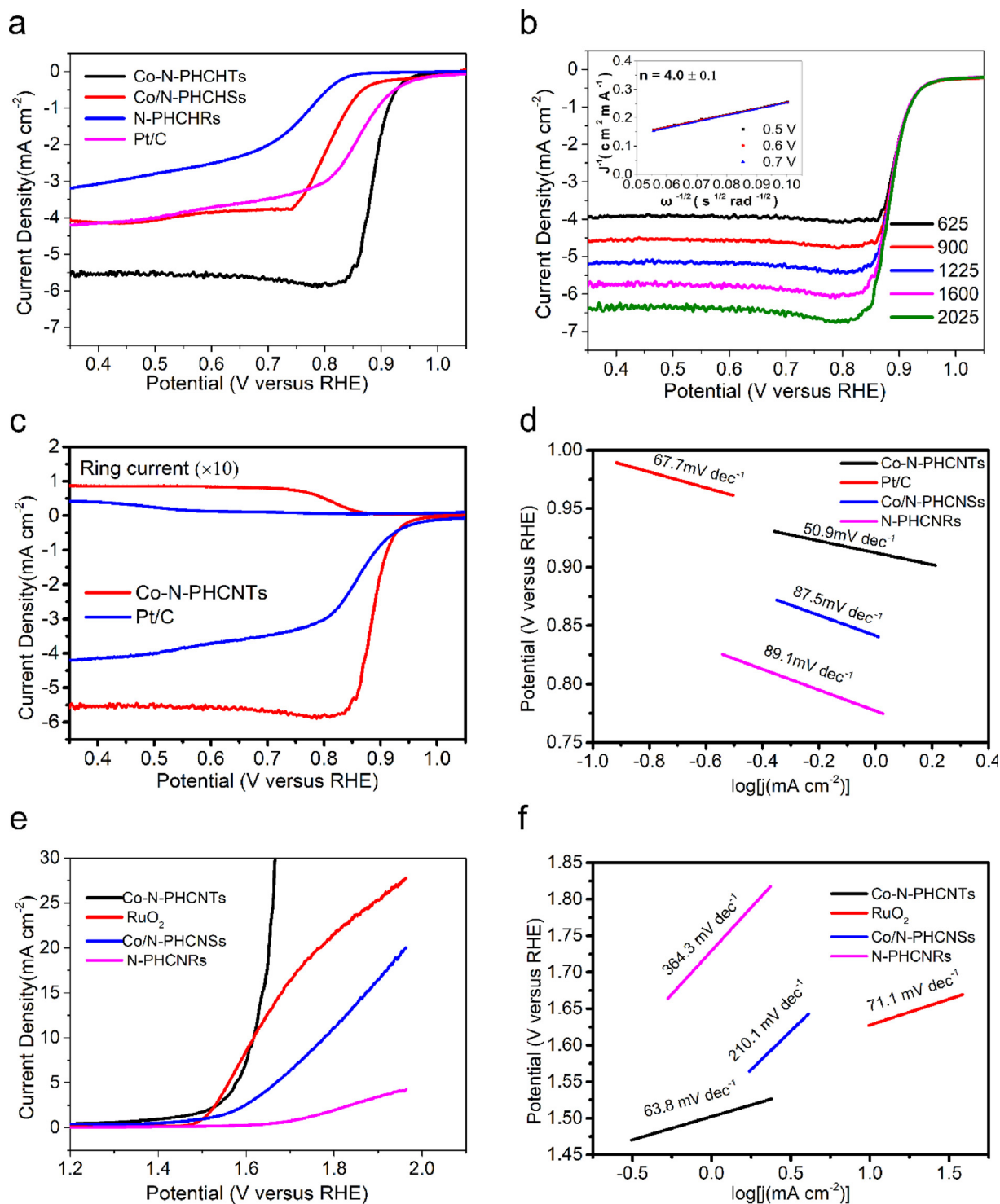
Fig. 3. (a) LSV curves of Co-*N*-PHCNTs, Co/N-PHCNSs, N-PHCNRs and Pt/C in 0.1 M KOH at 1600 rpm at a scan rate of 5 mV s^{-1}, (b) LSV curves of the Co-*N*-PHCNT electrocatalyst at various rotation rate and the inset is the corresponding K–L plot, (c) The high diffusion-limited current densities and low ring current densities (×10) of Co-*N*-PHCNTs and Pt/C, (d) The ORR Tafel plots of Co-*N*-PHCNTs, Co/N-PHCNSs, N-PHCNRs and Pt/C, (e) LSV curves of Co-*N*-PHCNTs, Co/N-PHCNSs, N-PHCNRs and RuO$_2$ for the OER at 1600 rpm in 0.1 M KOH at a scan rate of 5 mV s^{-1}, and (f) The OER Tafel plots of Co-*N*-PHCNTs, Co/N-PHCNSs, N-PHCNRs and RuO$_2$.

Fig. 2**d** illustrates the N$_2$ adsorption/desorption isotherms of Co-*N*-PHCNTs, N-PHCNRs and Co/N-PHCNSs, which demonstrate a type IV isotherm with a significant hysteresis loop, suggesting the existence of a mesoporous structure [58]. Furthermore, the Co-*N*-PHCNTs have the largest specific surface area (411 m^2 g^{-1}) among the three products (29.2 m^2 g^{-1} for Co/N-PHCNSs and 167 m^2 g^{-1} for N-PHCNRs). This

can be attributed to the unique structure of the carbon nanotubes derived from the nanosheet, which significantly increases its specific surface area. In addition, the Co-*N*-PHCNTs have a typical mesoporous structure with an average pore size of ˜4 nm, as shown in Fig. 2e. This large specific surface area and mesoporous distribution for Co-*N*-PHCNTs contribute substantially to the effectiveness of the three-phase
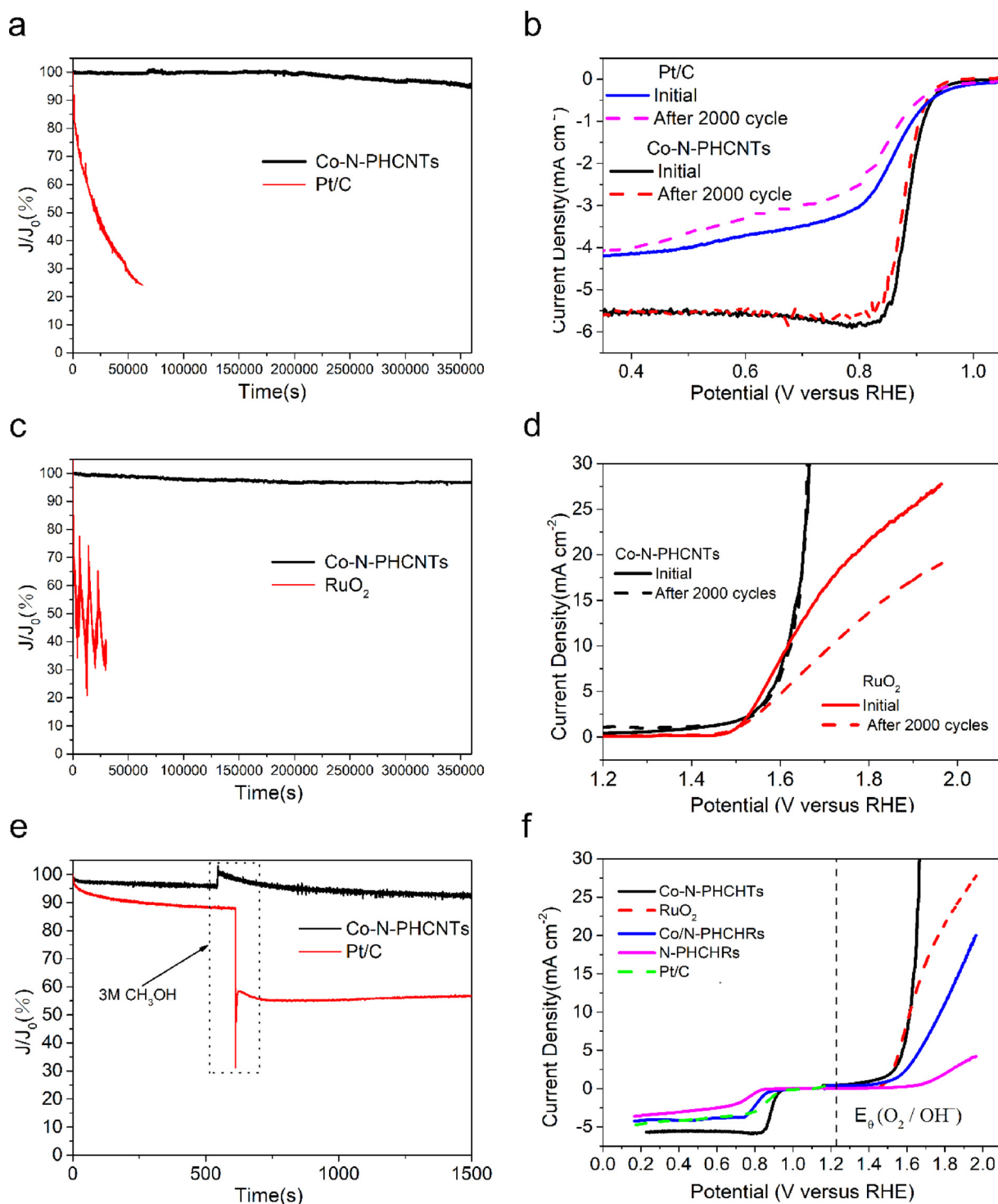
Fig. 4. (a)The i–t chronoamperometric response at 0.8 V vs. RHE for 360,000 s for Co-*N*-PHCNTs and Pt/C, (b) LSV curves of Co-*N*-PHCNTs and Pt/C before and after 2 000 potential cycles at a potential range of 0.4–1.0 V versus RHE and a sweep speed of 100 mV s^{-1}, (c) The i–t chronoamperometric response at 1.6 V vs. RHE for 360,000 s for Co-*N*-PHCNTs and RuO$_2$, (d) LSV curves of Co-*N*-PHCNTs and RuO$_2$ before and after 2 000 potential cycles at a potential range of 1.2–1.8 V versus RHE with a sweep speed of 100 mV s^{-1}, (e) Chronoamperometric response at 0.8 V after the introduction of 3 M methanol into 65 mL of 0.1 M KOH solution for Co-*N*-PHCNTs and Pt/C, and (f) LSV curves of different electrocatalysts for both the ORR and the OER in O$_2$-saturated 0.1 M KOH at 1600 rpm. For all LSV curves, the scan rate is 5 mV s^{-1}.

reaction interfaces. [59,60]

3.2. Electrochemical evaluation

To evaluate the electrocatalytic performance of the Co-*N*-PHCNTs, linear sweep voltammetry (LSV) measurements were adopted. Fig. 3a

illustrates that the Co-*N*-PHCNTs exhibited excellent ORR activity with a more positive onset potential ($E_{onset} \approx 0.98$ V) than both Co/N-PHCNSs ($E_{onset} \approx 0.92$ V) and N-PHCHRs ($E_{onset} \approx 0.87$ V). In addition, the half-wave potential for Co-*N*-PHCNTs ($E_{1/2} \approx 0.89$ V) is also more positive than those of Pt/C ($E_{1/2} \approx 0.87$ V), Co/N-PHCNSs ($E_{1/2} \approx 0.81$ V) and N-PHCHRs ($E_{1/2} \approx 0.76$ V). To further investigate the

effect of morphology and the metal ion ratio on electrocatalytic activity, the electrochemical performance of final products derived from the different Co/Zn molar ratios was measured (**Fig. S13a**). Moreover, the electrochemical performance of the Co-*N*-PHCNTs without PVP, Co/N/CNT and the product derived from Co/Zn ZIF-L was also investigated. The results demonstrated that the pyrolysis product displays a worse electrocatalytic activity than the Co-*N*-PHCNTs, which were capable of maintaining their morphology during pyrolysis (**Fig. S13b**).

Although Co/Zn (1:2) ZIF-PHS has a regular encapsulating microstructure with uniformly dispersed Co-*N*-C active sites, the lower CNT and Co contents cause relatively poor electrocatalytic activity. Co/Zn (2:1) ZIF-PHS has poor electrochemical performance due to the aggregation of the Co nanoparticles despite its regular encapsulating microstructure and the CNTs distributed on the surface. Additionally, when the molar ratio of Co/Zn changes to 1:4, the electrocatalyst derived from it shows poor electrocatalytic performance since the pine-cone-like structure formed by agglomeration and accumulation of fine layers has poor electrical conductivity, and the low Co content also leads to the loss of active sites. This finding is also in good agreement with the XPS results (**Fig. S14**).

By means of the K–L equation, the electron transfer number per oxygen molecule (n) for the ORR can be evaluated from the LSV plots at potentials from 0.5 to 0.7 V, which can assess the electrocatalytic kinetics [61]. For the Co-*N*-PHCNTs, the outstanding electrocatalytic performance can be demonstrated, suggesting a four-electron pathway for the ORR (n $\approx$ 4.0) (Fig. 3b). In addition, the high diffusion-limited current density of 5.52 mA cm^{-2} for the ORR and the low ring current density of 0.00873 mA cm^{-2} for the peroxide oxidation reaction also indicate that Co-*N*-PHCNTs are excellent electrocatalysts compared to Pt/C (Fig. 3c). Furthermore, **Fig. S15** illustrates the percentage of peroxide species relative to total oxygen reduction products and the electron transfer numbers calculated from the ring current plots. The dependence of the transfer number on various mass-loadings is shown in **Fig. S16**. The RRDE test results reveal that the ORR occurs via a four-electron pathway (n is greater than 3.9) with the production of very few hydrogen peroxide species (less than 7%), which is consistent with the calculation results of the K–L equation. Additionally, the corresponding Tafel slopes of Co-*N*-PHCNTs, Co/N-PHCNSs, N-PHCNRs and Pt/C are calculated to be 50.9, 87.5, 89.1 and 67.7 mV dec^{-1}, respectively, which indicates the most rapid ORR kinetics of the Co-*N*-PHCNTs, superior to the state-of-the-art benchmark noble-metal Pt/C electrocatalyst (Fig. 3d).

The OER activity of Co-*N*-PHCNTs and commercial RuO$_2$ were investigated by LSV, as shown in Fig. 3e. The Co-*N*-PHCNTs have an overpotential of ~390 mV at a current of 10 mA cm^{-2}, which is lower than those of the other products derived from ZIF-PHS with different Co/Zn molar ratios (**Fig. S17a**), Co/N/CNT and the Co/Zn ZIF-L electrocatalysts (**Fig. S17b**) and comparable to that of RuO$_2$. Fig. 3f demonstrates that Co-*N*-PHCNTs (63.8 mV dec^{-1}) have a lower Tafel slope than Co/N-PHCNSs (210.1 mV dec^{-1}), N-PHCNRs (364.3 mV dec^{-1}) and RuO$_2$ (71.1 mV dec^{-1}), which confirms the optimized OER kinetics. The outstanding OER performance can be attributed to the exposure of a large number of Co-*N*-C active sites and the unique structure of the nanosheet derived carbon nanotubes, which increases the specific surface area and facilitates the transport of reactants.

To further understand the excellent electrochemical properties of the Co-*N*-PHCNT electrocatalyst, the effective electrochemical active surface area (ECSA) was estimated. As shown in **Fig. S18**, the Co-*N*-PHCNTs have a larger C$_{dl}$ value (28.36 m F cm^{-2}) than the Co-*N*-PHCNTs-1:4 (10.19 m F cm^{-2}), and Co-*N*-CNT (17.23 m F cm^{-2}). Thus, it can be concluded that with the unique morphology of the regular hexagonal porous carbon nanosheet with the carbon nanotubes grown from it, the Co-*N*-PHCNT material not only has a larger specific surface area but also possesses a larger effective electrochemical active surface area than other electrocatalysts derived from 2D MOFs, thereby resulting in superior electrochemical performance (**Table S2**).

The durability of Co-*N*-PHCNTs and noble-metal benchmarks was investigated by using the chronoamperometric response. For the ORR, the experiments were carried out at 0.7 V for an extended period of 360,000 s [62]. The Co-*N*-PHCNTs exhibited great long-term stability, which maintained 95% of the initial ORR current and was superior to commercial that of Pt/C (Fig. 4a). Furthermore, the stability was also evaluated in an O$_2$-saturated electrolyte at 100 mV s^{-1} in the potential window of 0.4–1.0 V. The Co-*N*-PHCNTs have very little activity attenuation ($\triangle$E$_{1/2}$ $\approx$ 5 mV) after 2000 cycles and are much better than Pt/C ($\triangle$E$_{1/2}$ $\approx$ 30 mV), as shown in Fig. 4**b**. For the OER tests, the chronoamperometric response at 1.6 V for an extended period of 360,000 s was evaluated. The Co-*N*-PHCNTs retained 98% of the initial OER current, superior to commercial RuO$_2$ (Fig. 4c). In addition, there is almost no attenuation for Co-*N*-PHCNTs over 2000 cycles at 100 mV s^{-1} in the potential window of 1.2–1.8 V, which is better than commercial RuO$_2$, as shown in Fig. 4d. Additionally, the Co-*N*-PHCNTs also displayed a higher resistance to the methanol and CO relative to the commercial Pt/C (Fig. 4e and **S19**). The properties of the bifunctional electrocatalyst can be determined by the variance of the OER potential at 10 mA cm^{-2} and the ORR E$_{1/2}$ ($\triangle$E = E$_{j=10}$-E$_{1/2}$) [63]. Fig. 4f and **Table S3** indicate that the Co-*N*-PHCNTs present the smallest $\triangle$E of approximately 0.73 V among the other ZIF-PHS-derived products and the noble metal benchmarks. In addition, the Co-*N*-PHCNTs can be considered as one of the well-developed bifunctional oxygen electrocatalysts that outperform most of the N-doped cobalt carbon materials, as shown in Table S4.

3.3. Performance of primary and rechargeable Zn–Air batteries

For practical applications, the Co-*N*-PHCNTs were applied as bifunctional air electrodes in zinc-air batteries (Fig. 5a). The commercial Pt/C and RuO$_2$ were mechanically mixed (mass ratio = 1:1) as the reference [64]. Fig. 5**b** illustrates that the Co-*N*-PHCNTs present a higher open circuit voltage of 1.4 V than the reference (1.36 V) and demonstrate more ideal charge and discharge curves at relatively high current densities. As shown in Fig. 5c, the Co-*N*-PHCNT electrode presents a high peak power density of $\approx$ 125.41 mW cm^{-2} at a current density of $\approx$130 mA cm^{-2}, which is superior to that of the reference (~95.09 mW cm^{-2} at a current density of $\approx$127.4 mA cm^{-2}). The galvanostatic charge–discharge at a current density of 5 mA cm^{-2} was also used to evaluate the zinc-air battery. It is shown that the Pt/C + RuO$_2$ reference displays a highly significant polarization after 268 charge/discharge cycles for 95 h (Fig. 5d), while for the Co-*N*-PHCNTs electrode, there are almost no voltage changes over 2000 charge/discharge cycles (for nearly 673 h) (Fig. 5e). In addition, the Co-*N*-PHCNTs show a low charge/discharge gap of 0.796 V, which is smaller than that of the commercial reference ($\approx$1.094 V). Moreover, at a high current density of 10 mA cm^{-2}, the Zn–air battery with a Co-*N*-PHCNT air cathode still presents superior electrochemical performance and is capable of providing a narrow charge/discharge gap of 1.0 V after 825 cycles for 275 h (**Fig. S20**). Furthermore, the electrochemical impedance spectroscopy (EIS) was also used to demonstrate the Zn–air battery with a Co-*N*-PHCNT air cathode displayed smaller interfacial and charge transfer resistances than the reference Pt/C + RuO$_2$ as shown in **Fig. S21**. The Co-*N*-PHCNTs maintained the positive-hexagon-shaped nanosheet morphology after the charge/discharge cycling test, as confirmed by TEM and HRTEM (**Fig. S22**). In addition, the XRD and XPS analysis also suggested the chemical states after electrochemical testing are nearly not changed, demonstrating the good stability of the Co-*N*-PHCNTs electrocatalyst. This may attribute to the well-designed structure which prevents the Co nanoparticles from leaching and aggregating by covering with a carbon layer (**Fig. S23**). Table S5 illustrates that the Co-*N*-PHCNT electrode-based Zn–air battery is one of the most stable rechargeable Zn–air batteries recently reported.

As specially prepared bifunctional electrocatalysts, Co-*N*-PHCNTs present superior activity and excellent long-term stability. These great
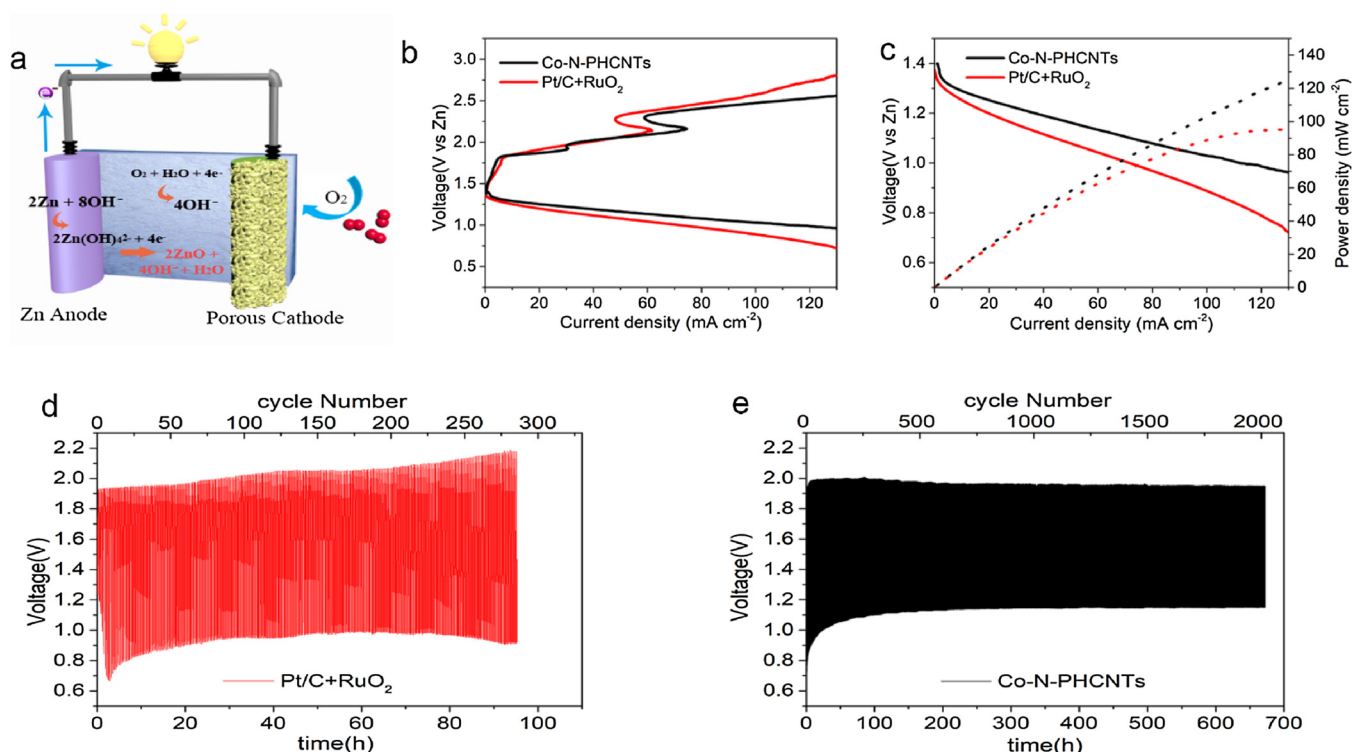
Fig. 5. (a) Schematic illustration of the Zn–air battery configuration, (b) charge and discharge polarization curves, (c) discharge polarization curves and the corresponding power density plots for the Zn–air batteries with Co-*N*-PHCNTs and Pt/C + RuO₂ electrocatalysts. Galvanostatic cycling stability tests of the Zn–air battery with (d) the noble-metal Pt/C + RuO₂ and (e) Co-*N*-PHCNT electrocatalysts at a current density of 5 mA cm^{-2}.

performances can be attributed to the following reasons: (i) the synergetic effect of the pyridinic and graphitic nitrogen in carbon lattice and the encapsulated transition metal nanoparticles improve the intrinsic electrocatalytic activity, and the higher degree of graphitization induced by the Co species was contributing to charge transfer throughout the electrocatalyst [65,66]; (ii) the well-designed structure prevents the Co nanoparticles from leaching and aggregating by covering with a carbon layer, which makes the electrocatalyst extremely stable and highly conductive; (iii) the regular hexagonal porous carbon nanosheet coated with carbon nanotubes allows the electrocatalyst to have a large specific surface area and effective electrochemical active surface area, which contribute substantially to diffusion of the reactants and efficient mass transfer; (iv) the strong covalent bonds between Co and N prevents collapse of the electrocatalyst morphology, ensuring the activity and durability of the Co-*N*-PHCNTs.

4. Conclusions

In summary, we developed a facile, low-cost, and scalable bottom-up method, i.e., a surfactant-assisted synthetic method, to prepare Co-*N*-PHCNTs. It is worth mentioning that during the pyrolysis procedure, the cohesive interactions between the selected surfactant and Co/Zn ZIF-PHS lead to a unique confinement effect to avoid collapse of the two-dimensional regular hexagonal layer structure derived from Co/Zn ZIF-PHS while also mitigating the agglomeration of neighbouring Co nanoparticles. The Co-*N*-PHCNTs pyrolyzed by 2D ZIF-PHS show a unique morphology of positive-hexagon-shaped nanosheets covered with carbon nanotubes, exhibiting a larger specific surface area and effective electrochemical active surface area. In addition, as an electrocatalyst, Co-*N*-PHCNT displays superior activities for the ORR and OER as well as excellent long-term stability and anti–toxic performance. Furthermore, Co-*N*-PHCNTs also acts as a remarkable bifunctional air electrode for rechargeable Zn–air batteries, which display a high peak power density of ≈ 125.41 mW cm^{-2} at a current density of ≈130 mA

cm^{-2}. After 2000 charge/discharge cycles (for nearly 673 h), there is no significant attenuation for the voltage gap, which displays exceptional long-term stability. This finding could pave a new path for the design of two-dimensional materials for electrocatalyst and energy storage as well as other fields.

Acknowledgements

Appendix A. Supplementary data

Supplementary material related to this article can be found, in the online version, at doi:https://doi.org/10.1016/j.apcatb.2019.117871.

References

[1] Z.W. Seh, J. Kibsgaard, C.F. Dickens, I. Chorkendorff, J.K. Norskov, T.F. Jaramillo, Combining theory and experiment in electrocatalysis: insights into materials design, Science 355 (2017) 4998.
[2] Z.P. Cano, D. Banham, S. Ye, A. Hintennach, J. Lu, M. Fowler, Z. Chen, Batteries and fuel cells for emerging electric vehicle markets, Nat. Energy 3 (2018) 279–289.
[3] J.F. Parker, C.N. Chervin, I.R. Pala, M. Machler, M.F. Burz, J.W. Long, D.R. Rolison, Rechargeable nickel–3D zinc batteries: an energy-dense, safer alternative to lithium-ion, Science 356 (2017) 415.
[4] C.-Y. Su, H. Cheng, W. Li, Z.-Q. Liu, N. Li, Z. Hou, F.-Q. Bai, H.-X. Zhang, T.-Y. Ma, Atomic modulation of FeCo-nitrogen-carbon bifunctional oxygen electrodes for rechargeable and flexible all-solid-state zinc-air battery, Adv. Energy Mater. 7 (2017) 1602420.
[5] X. Ren, M. Huang, S. Luo, Y. Li, L. Deng, H. Mi, L. Sun, P. Zhang, PdNi alloy decorated 3D hierarchically N, S co-doped macro–mesoporous carbon composites as efficient free-standing and binder-free electrocatalysts for Li–O₂ batteries, J. Mater. Chem. A 6 (2018) 10856–10867.
[6] C. Li, M. Wu, R. Liu, High-performance bifunctional oxygen electrocatalysts for

zinc-air batteries over mesoporous Fe/Co-N-C nanofibers with embedding FeCo alloy nanoparticles, Appl. Catal. B Environ. 244 (2019) 150–158.

[7] W. Wan, X. Liu, H. Li, X. Peng, D. Xi, J. Luo, 3D carbon framework-supported CoNi nanoparticles as bifunctional oxygen electrocatalyst for rechargeable Zn-air batteries, Appl. Catal. B Environ. 240 (2019) 193–200.

[8] H. Cheng, M.-L. Li, C.-Y. Su, N. Li, Z.-Q. Liu, Cu-Co bimetallic oxide quantum dot decorated nitrogen-doped carbon nanotubes: a high-efficiency bifunctional oxygen electrode for Zn-air batteries, Adv. Funct. Mater. 27 (2017) 1701833.

[9] Y. Li, H. Dai, Recent advances in zinc-air batteries, Chem. Soc. Rev. 43 (2014) 5257–5275.

[10] J.-S. Lee, S. Tai Kim, R. Cao, N.-S. Choi, M. Liu, K.T. Lee, J. Cho, Metal-air batteries with high energy density: Li-air versus Zn-air, Adv. Energy Mater. 1 (2011) 34–50.

[11] W. Wan, X. Liu, H. Li, X. Peng, D. Xi, J. Luo, 3D carbon framework-supported CoNi nanoparticles as bifunctional oxygen electrocatalyst for rechargeable Zn-air batteries, Appl. Catal. B: Environ. 240 (2019) 193–200.

[12] H. Zhong, Q. Zhang, J. Wang, X. Zhang, X. Wei, Z. Wu, K. Li, F. Meng, D. Bao, J. Yan, Engineering ultrathin C3N4 quantum dots on graphene as a metal-free water reduction electrocatalyst, ACS Catal. 8 (2018) 3965–3970.

[13] X. Cui, P. Ren, D. Deng, J. Deng, X. Bao, Single layer graphene encapsulating non-precious metals as high-performance electrocatalysts for water oxidation, Energy Environ. Sci. 9 (2016) 123–129.

[14] C. Hu, L. Dai, Multifunctional carbon-based metal-free electrocatalysts for simultaneous oxygen reduction, oxygen evolution, and hydrogen evolution, Adv. Mater. 29 (2017) 1604942.

[15] C. Zhang, J. Zhang, J. Zhu, W. Li, Z. Kou, Y. Huang, In situ exfoliating and generating active sites on graphene nanosheets strongly coupled with carbon fiber toward self-standing bifunctional cathode for rechargeable Zn-air batteries, Adv. Energy Mater. 8 (2018) 1703539.

[16] J. Wang, D. Gao, G. Wang, S. Miao, H. Wu, J. Li, X. Bao, Cobalt nanoparticles encapsulated in nitrogen-doped carbon as a bifunctional electrocatalyst for water electrolysis, J. Mater. Chem. A 2 (2014) 20067–20074.

[17] Z. Chen, R. Wu, Y. Liu, Y. Ha, Y. Guo, D. Sun, M. Liu, F. Fang, Ultrafine Co nanoparticles encapsulated in carbon-nanotubes-grafted graphene sheets as advanced electrocatalysts for the hydrogen evolution reaction, Adv. Mater. 30 (2018) 1802011.

[18] C. Yan, Y. Zhu, Z. Fang, C. Lv, X. Zhou, G. Chen, G. Yu, Heterogeneous molten salt design strategy toward coupling cobalt-cobalt oxide and carbon for efficient energy conversion and storage, Adv. Energy Mater. 8 (2018) 1800762.

[19] T. Sun, J. Wang, C. Qiu, X. Ling, B. Tian, W. Chen, C. Su, B, N co-doped and defect-rich nanocarbon material as a metal-free bifunctional electrocatalyst for oxygen reduction and evolution reactions, Adv. Sci. 5 (2018) 1800036.

[20] B. Liu, H. Li, B. Cao, J. Jiang, R. Gao, J. Zhang, Few Layered N, P dual-doped carbon-encapsulated ultrafine MoP nanocrystal/MoP cluster hybrids on carbon cloth: An ultrahigh active and durable 3D self-supported integrated electrode for hydrogen evolution reaction in a wide pH range, Adv. Funct. Mater. 28 (2018) 1801527.

[21] X. Cai, B.Y. Xia, J. Franklin, B. Li, X. Wang, Z. Wang, L. Chen, J. Lin, L. Lai, Z. Shen, Free-standing vertically-aligned nitrogen-doped carbon nanotube arrays/graphene as air-breathing electrodes for rechargeable zinc–air batteries, J. Mater. Chem. A 5 (2017) 2488–2495.

[22] B.Y. Guan, L. Yu, X.W. Lou, A dual-metal–organic-framework derived electrocatalyst for oxygen reduction, Energy Environ. Sci. 9 (2016) 3092–3096.

[23] G. Li, S. Zhao, Y. Zhang, Z. Tang, Metal-organic frameworks encapsulating active nanoparticles as emerging composites for catalysis: recent progress and perspectives, Adv. Mater. 30 (2018) 1800702.

[24] A. Indra, T. Song, U. Paik, Metal organic framework derived materials: progress and prospects for the energy conversion and storage, Adv. Mater. 30 (2018) 1705146.

[25] N. Cheng, L. Ren, X. Xu, Y. Du, S.X. Dou, Recent development of zeolitic imidazolate frameworks (ZIFs) derived porous carbon based materials as electrocatalysts, Adv. Energy Mater. 8 (2018) 1801257.

[26] M. Zhao, Y. Wang, Q. Ma, Y. Huang, X. Zhang, J. Ping, Z. Zhang, Q. Lu, Y. Yu, H. Xu, Y. Zhao, H. Zhang, Ultrathin 2D metal-organic framework nanosheets, Adv. Mater. 27 (2015) 7372–7378.

[27] M. Zhao, Y. Huang, Y. Peng, Z. Huang, Q. Ma, H. Zhang, Two-dimensional metal-organic framework nanosheets: synthesis and applications, Chem. Soc. Rev. 47 (2018) 6267–6295.

[28] T. Wang, Z. Kou, S. Mu, J. Liu, D. He, I.S. Amiinu, W. Meng, K. Zhou, Z. Luo, S. Chaemchuen, F. Verpoort, 2D dual-metal zeolitic-imidazolate-framework-(ZIF)-derived bifunctional air electrodes with ultrahigh electrochemical properties for rechargeable zinc-air batteries, Adv. Funct. Mater. 28 (2017) 1705048.

[29] Y. Jiang, Y.-P. Deng, J. Fu, D.U. Lee, R. Liang, Z.P. Cano, Y. Liu, Z. Bai, S. Hwang, L. Yang, D. Su, W. Chu, Z. Chen, Interpenetrating triphase cobalt-based nanocomposites as efficient bifunctional oxygen electrocatalysts for long-lasting rechargeable Zn-air batteries, Adv. Energy Mater. 8 (2018) 1702900.

[30] Y. Jiang, H. Liu, X. Tan, L. Guo, J. Zhang, S. Liu, Y. Guo, J. Zhang, H. Wang, W. Chu, Monoclinic ZIF-8 nanosheet-derived 2D carbon nanosheets as sulfur immobilizer for high-performance lithium sulfur batteries, ACS Appl. Mater. Interfaces 9 (2017) 25239–25249.

[31] Y. Xu, B. Li, S. Zheng, P. Wu, J. Zhan, H. Xue, Q. Xu, H. Pang, Ultrathin two-dimensional cobalt–organic framework nanosheets for high-performance electrocatalytic oxygen evolution, J. Mater. Chem. A 6 (2018) 22070–22076.

[32] T. Rodenas, I. Luz, G. Prieto, B. Seoane, H. Miro, A. Corma, F. Kapteijn, I.X.F.X. Llabres, J. Gascon, Metal-organic framework nanosheets in polymer composite materials for gas separation, Nat. Mater. 14 (2015) 48–55.

[33] Y.B. Huang, J. Liang, X.S. Wang, R. Cao, Multifunctional metal-organic framework electrocatalysts: synergistic catalysis and tandem reactions, Chem. Soc. Rev. 46

[34] K. Jayaramulu, J. Masa, D. Morales, O. Tomanec, V. Ranc, M. Petr, P. Wilde, Y. Chen, R. Zboril, W. Schuhmann, R. Fischer, Ultrathin 2D cobalt zeolite-imidazole framework nanosheets for electrocatalytic oxygen evolution, Adv. Sci. 5 (2018) 1801029.

[35] G. Zhang, Y. Li, J. Gao, F. Zhang, Q. Qian, Y. Liu, Hierarchical 3D macrosheets composed of interconnected in-situ cobalt catalyzed nitrogen doped carbon nanotubes as superior bifunctional oxygen electrocatalysts for rechargeable Zn-air batteries, J. Mater. Chem. A 6 (2018) 15523–15529.

[36] Y. He, S. Hwang, D.A. Cullen, M.A. Uddin, L. Langhorst, B. Li, S. Karakalos, A.J. Kropf, E.C. Wegener, J. Sokolowski, M. Chen, D. Myers, D. Su, K.L. More, G. Wang, S. Litster, G. Wu, Highly active atomically dispersed CoN4 fuel cell cathode electrocatalysts derived from surfactant-assisted MOFs: carbon-shell confinement strategy, Energy Environ. Sci. 12 (2019) 250–260.

[37] Y. Pan, D. Heryadi, F. Zhou, L. Zhao, G. Lestari, H. Su, Z. Lai, Tuning the crystal morphology and size of zeolitic imidazolate framework-8 in aqueous solution by surfactants, CrystEngComm 13 (2011) 6937–6940.

[38] J. Zhao, Y. Wang, W. Dong, Y. Wu, D. Li, B. Liu, Q. Zhang, A new surfactant-introduction strategy for separating the pure single-phase of metal-organic frameworks, Chem. Commun. 51 (2015) 9479–9482.

[39] Z. Liang, C. Zhang, H. Yuan, W. Zhang, H. Zheng, R. Cao, PVP-assisted transformation of a metal–organic framework into Co-embedded N-enriched meso/microporous carbon materials as bifunctional electrocatalysts, Chem. Commun. 54 (2018) 7519–7522.

[40] Q. Lai, Y. Zhao, Y. Liang, J. He, J. Chen, In situ confinement pyrolysis transformation of ZIF-8 to nitrogen-enriched meso-microporous carbon frameworks for oxygen reduction, Adv. Funct. Mater. 26 (2016) 8334–8344.

[41] C. Zhu, Q. Shi, B.Z. Xu, S. Fu, G. Wan, C. Yang, S. Yao, J. Song, H. Zhou, D. Du, S.P. Beckman, D. Su, Y. Lin, Hierarchically porous M-N-C (M = Co and Fe) single-atom electrocatalysts with robust MNx active moieties enable enhanced ORR performance, Adv. Energy Mater. 8 (2018) 1801956.

[42] T. Palaniselvam, V. Kashyap, S.N. Bhange, J.-B. Baek, S. Kurungot, Nanoporous graphene enriched with Fe/Co-N active sites as a promising oxygen reduction electrocatalyst for anion exchange membrane fuel cells, Adv. Funct. Mater. 26 (2016) 2150–2162.

[43] Z. Kou, T. Meng, B. Guo, I.S. Amiinu, W. Li, J. Zhang, S. Mu, A generic conversion strategy: from 2D metal carbides (MxCy) to M-self-doped graphene toward high-efficiency energy applications, Adv. Funct. Mater. 27 (2017) 1604904.

[44] Y. Ye, F. Cai, H. Li, H. Wu, G. Wang, Y. Li, S. Miao, S. Xie, R. Si, J. Wang, X. Bao, Surface functionalization of ZIF-8 with ammonium ferric citrate toward high exposure of Fe-N active sites for efficient oxygen and carbon dioxide electroreduction, Nano Energy 38 (2017) 281–289.

[45] Y. Pan, K. Sun, S. Liu, X. Cao, K. Wu, W.C. Cheong, Z. Chen, Y. Wang, Y. Li, Y. Liu, D. Wang, Q. Peng, C. Chen, Y. Li, Core-shell ZIF-8@ZIF-67 derived CoP nanoparticles-embedded N-doped carbon nanotube hollow polyhedron for efficient overall water splitting, J. Am. Chem. Soc. 7 (2018) 2610–2618.

[46] S. Gao, Y. Lin, X. Jiao, Y. Sun, Q. Luo, W. Zhang, D. Li, J. Yang, Y. Xie, Partially oxidized atomic cobalt layers for carbon dioxide electroreduction to liquid fuel, Nature 529 (2016) 68–71.

[47] R. Chen, J. Yao, Q. Gu, S. Smeets, C. Baerlocher, H. Gu, D. Zhu, W. Morris, O.M. Yaghi, H. Wang, A two-dimensional zeolitic imidazolate framework with a cushion-shaped cavity for CO2 adsorption, Chem. Commun. 49 (2013) 9500–9502.

[48] P. Matousek, N. Stone, Development of deep subsurface Raman spectroscopy for medical diagnosis and disease monitoring, Chem. Soc. Rev. 45 (2016) 1794–1802.

[49] Z. Kou, B. Guo, Y. Zhao, S. Huang, T. Meng, J. Zhang, W. Li, I.S. Amiinu, Z. Pu, M. Wang, M. Jiang, X. Liu, Y. Tang, S. Mu, Molybdenum carbide-derived chlorine-doped ordered mesoporous carbon with few-layered graphene walls for energy storage applications, ACS Appl. Mater. Interfaces 9 (2017) 3702–3712.

[50] Y. Qian, Z. Liu, H. Zhang, P. Wu, C. Cai, Active site structures in nitrogen-doped carbon-supported cobalt electrocatalysts for the oxygen reduction reaction, ACS Appl. Mater. Interfaces 8 (2016) 32875–32886.

[51] J. Yu, G. Chen, J. Sunarso, Y. Zhu, R. Ran, Z. Zhu, W. Zhou, Z. Shao, Cobalt oxide and cobalt-graphitic carbon core-shell based electrocatalysts with remarkably high oxygen reduction reaction activity, Adv. Sci. 3 (2016) 1600060.

[52] J. Jiang, Q. Liu, C. Zeng, L. Ai, Cobalt/molybdenum carbide@N-doped carbon as a bifunctional electrocatalyst for hydrogen and oxygen evolution reactions, J. Mater. Chem. A 5 (2017) 16929–16935.

[53] P. Yin, T. Yao, Y. Wu, L. Zheng, Y. Lin, W. Liu, H. Ju, J. Zhu, X. Hong, Z. Deng, G. Zhou, S. Wei, Y. Li, Single cobalt atoms with precise N-Coordination as superior oxygen reduction reaction electrocatalysts, Angew. Chem., Int. Ed. 55 (2016) 10800–10805.

[54] K. Gong, F. Du, Z. Xia, M. Durstock, L. Dai, Nitrogen-doped carbon nanotube arrays with high electrocatalytic activity for oxygen reduction, Science 323 (2009) 760.

[55] A. Morozan, P. Jegou, B. Jousselme, S. Palacin, Electrochemical performance of annealed cobalt-benzotriazole/CNTs electrocatalysts towards the oxygen reduction reaction, Phys. Chem. Chem. Phys. 13 (2011) 21600–21607.

[56] J. Masa, W. Xia, I. Sinev, A. Zhao, Z. Sun, S. Grützke, P. Weide, M. Muhler, W. Schuhmann, MnxOy/NC and CoxOy/NC nanoparticles embedded in a nitrogen-doped carbon matrix for high-performance bifunctional oxygen electrodes, Angew. Chem. Int. Ed. 53 (2014) 8508–8512.

[57] I.S. Amiinu, X. Liu, Z. Pu, W. Li, Q. Li, J. Zhang, H. Tang, H. Zhang, S. Mu, From 3D ZIF nanocrystals to Co-Nx/C nanorod array electrocatalysts for ORR, OER, and Zn-air batteries, Adv. Funct. Mater. 28 (2018) 1704638.

[58] J. Liu, M. Zheng, J. Shi, H. Zeng, H. Xia, Amorphous FeOOH quantum dots assembled mesoporous film anchored on graphene nanosheets with superior electrochemical performance for supercapacitors, Adv. Funct. Mater. 26 (2016)

919–930.

[59] S. Chen, L. Zhao, J. Ma, Y. Wang, L. Dai, J. Zhang, Edge-doping modulation of N, P-codoped porous carbon spheres for high-performance rechargeable Zn-air batteries, Nano Energy 60 (2019) 536–544.

[60] W. Zhang, Z.Y. Wu, H.L. Jiang, S.H. Yu, Nanowire-directed templating synthesis of metal-organic framework nanofibers and their derived porous doped carbon na-nofibers for enhanced electrocatalysis, J. Am. Chem. Soc. 136 (2014) 14385–14388.

[61] M.K. Debe, Electrocatalyst approaches and challenges for automotive fuel cells, Nature 486 (2012) 43–51.

[62] S.S. Shinde, C.H. Lee, J.-Y. Jung, N.K. Wagh, S.-H. Kim, D.-H. Kim, C. Lin, S.U. Lee, J.-H. Lee, Unveiling dual-linkage 3D hexaiminobenzene metal–organic frameworks towards long-lasting advanced reversible Zn–air batteries, Energy Environ. Sci. 12 (2019) 727–738.

[63] Y. Huang, Y. Wang, C. Tang, J. Wang, Q. Zhang, Y. Wang, J. Zhang, Atomic modulation and structure design of carbons for bifunctional electrocatalysis in metal-air batteries, Adv. Mater. 31 (2018) 1803800.

[64] G. Fu, J. Wang, Y. Chen, Y. Liu, Y. Tang, J.B. Goodenough, J.-M. Lee, Exploring indium-based ternary thiospinel as conceivable high-potential air-cathode for re-chargeable Zn-air batteries, Adv. Energy Mater. 8 (2018) 1802263.

[65] D. Deng, L. Yu, X. Chen, G. Wang, L. Jin, X. Pan, J. Deng, G. Sun, X. Bao, Iron encapsulated within pod-like carbon nanotubes for oxygen reduction reaction, Angew. Chem. Int. Ed. 52 (2013) 371–375.

[66] J. Wang, D. Gao, G. Wang, S. Miao, H. Wu, J. Li, X. Bao, Cobalt nanoparticles encapsulated in nitrogen-doped carbon as a bifunctional electrocatalyst for water electrolysis, J. Mater, Chem. A. 2 (2014) 20067–20074.